Using the Translation Speed and Vertical Structure of Gust Fronts to Infer Buoyancy Deficits within Thunderstorm Outflow

ABBY HUTSON AND CHRISTOPHER WEISS

Texas Tech University, Lubbock, Texas

GEORGE BRYAN

NCAR/UCAR, Boulder, Colorado

(Manuscript received 12 December 2018, in final form 3 July 2019)

ABSTRACT

This study investigates whether the thermodynamics of supercell rear-flank outflow can be inferred from the propagation speed and vertical structure of the rear-flank gust front. To quantify the relationship between outflow thermodynamic deficit and gust front structure, CM1 is applied as a two-dimensional cold pool model to assess the vertical slope of cold pools of varying strength in different configurations of ambient shear. The model was run with both free-slip and semislip lower boundary conditions and the results were compared to observations of severe thunderstorm outflow captured by the Texas Tech University Ka-band mobile radars. Simulated cold pools in the free-slip model achieve the propagation speeds predicted by cold pool theory, while cold pool speeds in the semislip model propagate slower. Density current theory is applied to the observed cold pools and predicts the cold pool speed to within about 2 m s^{-1}. Both the free-slip and semislip model results reveal that, in the same sheared flow, the edge of a strong cold pool is less inclined than that of a weaker cold pool. Also, a cold pool in weak ambient shear has a steeper slope than the same cold pool in stronger ambient shear. Nonlinear regressions performed on data from both models capture the proper dependence of slope on buoyancy and shear, but the free-slip model does not predict observed slopes within acceptable error, and the semislip model overpredicts the cold pool slope for all observed cases, but with uncertainty due to shear estimation.

1. Introduction

In prior studies of supercell structure and evolution, the rear-flank downdraft (RFD) has emerged as an important feature with regards to tornadogenesis (e.g., Lemon and Doswell 1979; Rotunno and Klemp 1985; Dowell and Bluestein 1997; Adlerman et al. 1999; Markowski 2002; Markowski et al. 2002; Beck et al. 2006; Grzych et al. 2007; Hirth et al. 2008; Markowski et al. 2008; Finley and Lee 2008; Markowski and Richardson 2009; Marquis et al. 2012; Beck and Weiss 2013; Skinner et al. 2014). This mass of descending air on the back side of a supercell updraft is theorized to play several roles in the generation of a tornado, including the advection of vertical vorticity toward the surface and providing a mechanism for convergence and vortex stretching along the leading edge of the outflow, the rear-flank gust front (RFGF; Klemp et al. 1981; Davies-Jones 1982; Davies-Jones and Brooks 1993; Dowell and Bluestein 1997; Adlerman et al. 1999; Davies-Jones et al. 2001; Markowski 2002; Beck et al. 2006; Markowski et al. 2008; Marquis et al. 2008), as well as being a source for baroclinic vorticity generation (Klemp and Rotunno 1983; Rotunno and Klemp 1985; Markowski 2002; Markowski et al. 2008; Beck and Weiss 2013; Skinner et al. 2015; Weiss et al. 2015).

RFDs are also considered to influence tornadogenesis through the modulation of buoyancy. Air parcels that enter the low-level updraft often traverse through the RFD near the surface and are influenced by the buoyancy of the RFD air, thus aiding tornadogenesis through increased stretching of vertical vorticity or inhibiting tornadogenesis by decreasing vertical acceleration, perhaps prohibiting ultimate achievement of the level of free convection altogether (Davies-Jones and Brooks 1993;

Denotes content that is immediately available upon publication as open access.

Corresponding author: Abby Hutson, abby.kenyon@ttu.edu

DOI: 10.1175/MWR-D-18-0439.1

Adlerman et al. 1999; Markowski 2002; Markowski et al. 2003; Markowski and Richardson 2009).

Past studies of tornadic and nontornadic RFDs have revealed a tangible link between a downdraft's characteristic buoyancy and tornado likelihood and intensity. Markowski et al. (2002) analyzed 30 different supercell cases from the original Verification of the Origin of Rotation in Tornadoes Experiment (VORTEX; Rasmussen et al. 1994) and subsequent campaigns. It was found that, in general, the smallest perturbations of equivalent potential temperature (θ_e) and virtual potential temperature (θ_v), relative to the base inflow state, were measured within RFDs of strongly tornadic storms (Fig. 1). Studies following the Markowski (2002) analysis supported that conclusion (Grzych et al. 2007; Hirth et al. 2008; Finley and Lee 2008; Skinner et al. 2014; Weiss et al. 2015). Some studies even recorded small θ_e excesses within RFD air close to tornado passage (Hirth et al. 2008; Weiss et al. 2015).

The collection of in situ measurements within the portion of the RFD nearest the tornado is both difficult and dangerous, raising the question of whether the thermodynamics of a supercell RFD can instead be inferred using remote sensing (i.e., mobile Doppler radar). This study evaluates the feasibility of such an approach, whereby observed RFGF shape and evolution can be related to the intrinsic buoyancy through density current theory.

The strength of a cold pool has been shown to influence both its propagation speed and its structure. The speed of a cold pool can be expressed using the following equation:

$$c = k\sqrt{gh\frac{\rho_1 - \rho_0}{\rho_0}}, \tag{1}$$

where c is the propagation speed of the cold pool, g is the acceleration due to gravity, h is the depth of the cold pool, ρ_0 is the air density of the environment, ρ_1 is the air density within the cold pool, and k is a variable often ranging between 0.7 and 1.3 that accounts for finite channel depth effects and viscous dissipation (Benjamin 1968; Bluestein 2013, 137–152; Markowski and Richardson 2014). The presence of environmental shear has been shown to affect the propagation speed of a cold pool (Simpson and Britter 1980; Xu 1992; Chen 1995; Xu et al. 1996; Liu and Moncrieff 1996). One way to include shear into the speed equation is

$$c = -\Delta u + k\sqrt{gh\frac{\rho_1 - \rho_0}{\rho_0}}, \tag{2}$$

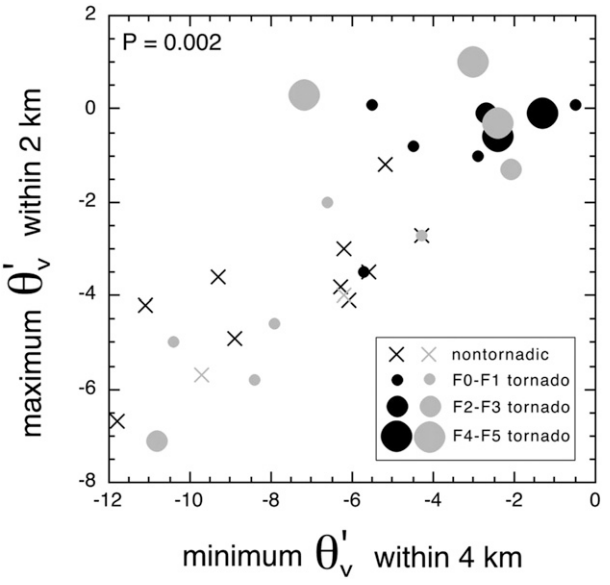

FIG. 1. A scatterplot of maximum θ_v vs minimum θ_v values recorded within RFDs of tornadic and nontornadic supercells in the original VORTEX project. Black (gray) symbols refer to cases in which analyses were (were not) obtained within 5 min of tornadogenesis or tornadogenesis failure. [From Markowski (2002).]

where Δu is the shear vector magnitude (vector difference between the wind at height h and the wind at the surface).

Defining cold pool structure (specifically, the shape of the leading edge) and how it is affected by cold pool strength is more complex. Environmental shear is the biggest factor affecting the structure of a cold pool (e.g., Rotunno et al. 1988; Xu 1992; Chen 1995; Liu and Moncrieff 1996; Bryan and Rotunno 2014b). Rotunno et al. (1988, hereafter RKW88) determined that cold pools in a sheared environment can have an "optimal state"—a state in which air is forced upward into a vertically oriented jet (Fig. 2). This vertical jet manifests itself in the shape of the cold pool edge—a cold pool in the optimal state has nearly a 90° slope.[1]

RKW88 determined the necessary conditions for the optimal state using a vorticity budget within a control volume (CV) around the cold pool edge:

$$0 = -\frac{\partial}{\partial t}\int_L^R\int_0^d \eta\, dx\, dz + \int_0^d (u\eta)_L\, dz - \int_0^d (u\eta)_R\, dz - \int_L^R (w\eta)_d\, dz + \int_0^d (B_L - B_R)\, dz, \tag{3}$$

[1] While the schematic in Fig. 2d does show a vertical jet, RKW88 did not determine the slope of the cold pool to reflect what it would look like in the optimal state. This shape was later determined by Bryan and Rotunno (2014b), Fig. 2.

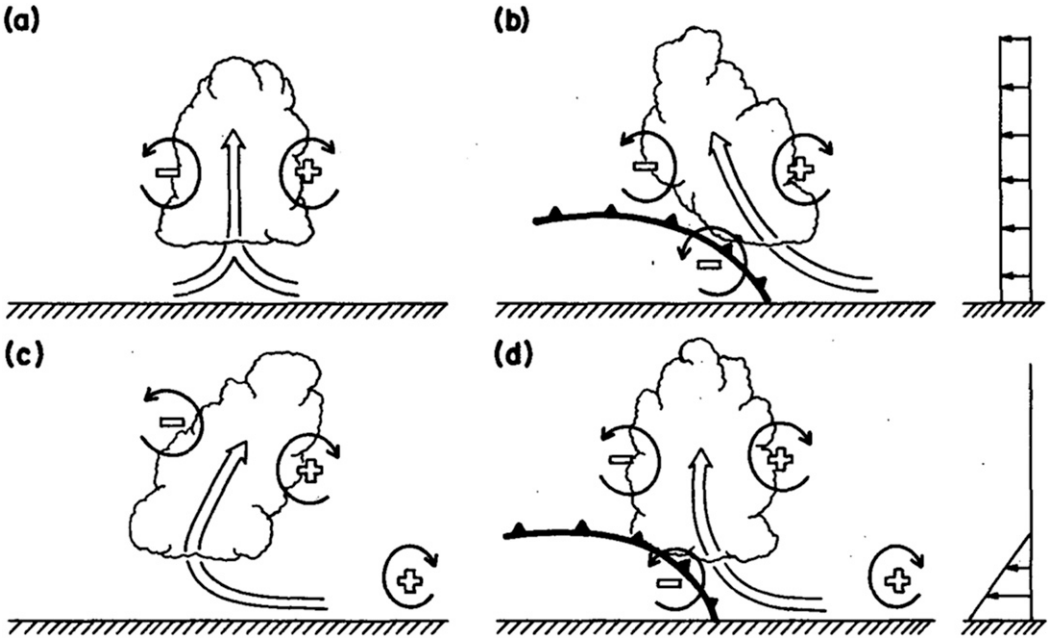

FIG. 2. A visual representation of RKW theory. (a) A convective updraft in uniform flow. (b) A convective updraft in uniform flow is tilted due to baroclinic vorticity generated by a cold pool. (c) A convective updraft in sheared flow tilts due to environmental horizontal vorticity. (d) A convective updraft is upright as baroclinic vorticity balances environmental horizontal vorticity produced by sheared flow. This is often referred to as the "optimal state" for long-lived convection. [From Rotunno et al. (1988).]

where R and L indicate the right and left edges of the CV, respectively; d refers to the domain depth; u is the horizontal wind; w is the vertical wind; B_x is buoyancy; and η is the total vorticity perpendicular to the CV plane. The first integral gives the net tendency of vorticity within the CV, the second, third, and fourth integrals give the vorticity flux at the left, right, and top boundaries, respectively; and the last integral in the equation gives the net buoyant generation of baroclinic vorticity in the CV. The buoyant generation of vorticity is determined by the density excess within the cold pool. RKW88 hypothesized that the net buoyant generation of negative vorticity is balanced by the import of positive vorticity from the low-level shear for a cold pool in the optimal state.

Bryan and Rotunno (2014b) used a numerical model to study the optimal state and verified the RKW88 hypothesis that environmental vorticity balances the baroclinic vorticity generated by the cold pool. In addition, Bryan and Rotunno (2014b) simulated cold pools in nonoptimal conditions by adjusting the cold pool deficit and the ambient shear independently. The results revealed that, in sheared flow, a decrease in cold pool temperature deficit produces a steeper slope while an increase in this deficit produces a shallower slope.

The purpose of this study is to determine how the speed and slope of a gust front is dependent on cold pool strength (defined by its potential temperature deficit) and whether that dependence can be observed. In principle, a gust front's structure, by virtue of its tie to outflow buoyancy, might be used to infer supercell tornadic potential. We expect that a cold pool with a stronger (weaker) buoyancy deficit will have more shallow (steep) leading edge vertical slope. A two-dimensional model is used to simulate and analyze various cold pool–environment interactions to test this hypothesis, the results of which are then compared to the observed speed and slope of cold pools sampled using Doppler radar.

2. Methods

a. Cold pool model

The model used in this study is a two-dimensional cold pool model developed and used by Bryan and Rotunno (2014a,b). It is a modified, two-dimensional version of Cloud Model, version 1 (CM1; Bryan and Fritsch 2002), with an x–z grid characterized with a 31.25 m grid spacing. The lateral boundaries have open boundary conditions while the upper and lower boundaries are flat and rigid. The upper boundary is free slip and is located eight times the initial cold pool height.

Both free-slip and semislip lower boundary conditions are used to study cold pool shape and propagation.

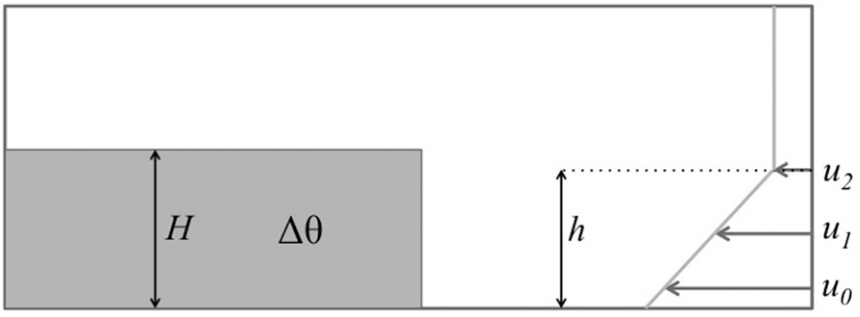

FIG. 3. A conceptual schematic showing the initialized state of the modified CM1 cold pool model. The shaded region indicates cold air with a potential temperature deficit $\Delta\theta$ and depth H. Ambient two-dimensional shear is defined with three specified wind speeds (u_x) at three different heights. The wind speed at the highest altitude indicated (u_2) is held constant through the upper depth of the domain; H and h, the depth of the sheared layer, do not need to be equal.

Friction is implemented on the lower boundary of the cold pool model through the use of a surface drag coefficient (C_d). For all simulations, C_d was set to 0.01, a value typical of cropland and tall grass fields. To maintain the near-surface flow and keep the environmental shear vector intact throughout the simulation, a force-restore term was added to the u-momentum equation (see Markowski 2016).

The cold pool is initialized as a rectangular block of relatively cold air over the left half of the domain with a depth H. On the right side of the domain, ambient flow is defined using wind speeds at three different heights. The wind at the top of the shear layer (at depth h) is held constant in the vertical throughout the rest of the domain (Fig. 3). While the overall domain was fixed, all analysis was conducted in a moving CV centered around the leading edge of the cold pool as it propagated toward the right side of the domain.

Different cold pools were modeled by varying the initial potential temperature deficit, $\Delta\theta$. The shape of these cold pools was then analyzed for different ambient shear profiles by changing the values for the wind at three different heights, u_0, u_1, and u_2. The wind in between the three designated levels was linearly interpolated to complete the shear profile. In total, 60 different combinations of $\Delta\theta$, shear strength (ΔU; the difference between u_2 and u_0), and shear depth (h/H; the height of the shear layer relative to the depth of the cold pool) were simulated using the free-slip model and 44 combinations were simulated using the semislip model. The detailed configurations of cold pool deficit, shear, and shear depth used to initialize the free-slip and semislip models can be found in Table 1.

To ensure limited temporal evolution of the environmental shear profile due to frictional drag, all semislip simulations were initiated with a shear profile in which the u component of the wind is $0\,\mathrm{m\,s^{-1}}$ at the lowest level and increases with height. This is in contrast to all free-slip simulations in which shear was modeled with a strong negative u-component wind (pointed toward the cold pool) at the lowest level that increased with height.

Cold pool speed and cold pool slope were the two dependent variables of interest after the model reached steady state. In a majority of cold pool studies (e.g., Benjamin 1968; Xue et al. 1997; Bryan and Rotunno 2014b; RKW88), calculations are performed using cold pool–relative flow, where the cold pool has no CV-relative motion and propagation speed is instead defined as the wind speed directly opposing the cold pool along the surface, or $c_{\mathrm{amb}} + \Delta u$, where c_{amb} is the ambient wind speed above the shear layer and Δu is the change in ambient wind speed within the shear layer [see Fig. 3.43 in Bluestein (2013, 137–152)]. In the cold pool model used in this study, the cold air does have ground-relative propagation, so cold pool speed was found by calculating the grid-relative propagation of the leading edge of cold air at the lowest model level, and then subtracting the grid-relative wind speed at the lowest model level (u_0). This ensured that any change in the ambient wind profile did not affect cold pool speed as long as the shear vector remained the same.

Cold pool slope is defined as the angle formed between the ground and the leading edge of the cold pool (on the cold side of the boundary), represented by the linear slope of the gust front between 250 and 750 m AGL. For cases in which the cold pool depth is less than 750 m, the cold pool slope is calculated between 0 and 500 m AGL. The averages of cold pool speed and slope between 30 and 45 min of simulation time were used to define the final values for the dependent variables to ensure that transient eddies did not affect the calculations.

TABLE 1. A table giving all of the combinations of cold pool deficit, shear, and shear depth used to initiate both the free-slip and semislip simulations; "F" indicates that combination of cold pool deficit and shear was used in the free-slip model with a shear depth of $1h/H$, and "S" indicates it was used in the same way for the semislip model. A boldface letter indicates that same combination was used with a shear depth of $2h/H$ as well as $1h/H$, and an italic letter indicates that same combination was also used with shear depths of $0.5h/H$ and $0.75h/H$.

	Shear	0 m s^{-1}	1 m s^{-1}	2 m s^{-1}	3 m s^{-1}	5 m s^{-1}	8 m s^{-1}	10 m s^{-1}	15 m s^{-1}
Cold pool deficit									
1.5 K		F S	F S	F	F S	**F S**	F **S**	***F S***	***F S***
3.0 K		F S	F S	F	F S	**F S**	F **S**	***F S***	***F S***
6.0 K		F S	F S	F	F S	**F S**	F **S**	***F S***	***F S***
8.0 K		F S	F S	F	F S	**F S**	F **S**	***F S***	***F S***

b. *Observational platforms*

Cold pool model results are compared to five different cold pools observed using various sampling platforms. Of the five cold pools, two are outflow associated with upscale, multicell thunderstorms (referred to as the Idalou and the Slaton multicell cases) and three are RFGFs from tornadic and nontornadic supercells (referred to as the OKV2, Hedley, and Tipton supercell cases).

The vertical structure of each cold pool was sampled using the Texas Tech University (TTU) Ka-band mobile Doppler radars (Gunter et al. 2015). Range–height indicator (RHI) scans were conducted to create a cross section of the gust front as it propagated forward. During each deployment, RHI azimuths were chosen by the radar operator to best intersect the gust front along a perpendicular plane. Radial velocity data—specifically, the location of the strongest radial velocity gradient indicating the boundary of the approaching cold air (as visible in the RHI)—were used for the slope and speed analysis of each cold pool. While the strongest radial velocity gradient was often associated with the zero isodop, there were instances in which the zero isodop was ambiguous below the lowest 1000 m, so using the strongest velocity gradient proved more consistent. Cold pool speed was estimated by tracking the distance traveled by the strongest velocity gradient along the surface in between scans and dividing that distance by the amount of time passed between scans. The speed calculations for each scan were then averaged over the entire deployment period to find one speed value for each case. To calculate cold pool slope, a linear gust front slope was calculated between 250 and 750 m AGL along the strongest velocity gradient across all cases. The results from each RHI scan during the deployment period (usually spaced about 1–2 min apart) were averaged to ensure that no transient eddies were affecting the slope calculation. While some cases involved longer deployments and different scan strategies than others, the amount of time over which RHIs were averaged was about 5 min, comprising of about 5–6 scans of the outflow. The actual slope of the cold pool was then defined as the angle between the ground and the linear slope of the inside edge of the cold pool.

Surface buoyancy deficits within each cold pool were measured using data from one of three different surface observing networks—the TTU StickNets (Schroeder and Weiss 2008; Weiss and Schroeder 2008), the West Texas Mesonet (Schroeder et al. 2005), and the Oklahoma Mesonet (Brock et al. 1995). All three networks measure temperature, relative humidity, and station pressure, all of which are used to calculate θ, θ_v, and θ_e [as shown by Bolton (1980)]. The West Texas Mesonet and the Oklahoma Mesonet record observations every five minutes; StickNets have a sampling frequency of 1 Hz. A time series from a single station was used to determine the thermodynamic deficit of the outflow in each of the observed cases. The base state is defined using the average potential temperature over 15 min, at least 5 min before the passage of the gust front. The cold pool deficit is defined as the greatest decrease of potential temperature during the first 15 min after gust front passage.

Two different methods are used to quantify the ambient shear opposing a cold pool. Wind speeds at different elevations are measured using velocity–azimuth displays (VADs) from the nearest WSR-88D,[2] and wind data from the North American Regional Reanalysis (NARR) are gathered over the grid point closest to the location of deployment. It is inherently assumed that the vertical wind profile at the VAD sites is the same as the vertical wind profile near the storm for all cases. There are clearly instances (e.g., the initiating boundary exists between the radar and the storm) where this assumption can be restrictive. To better represent the low-level shear with this technique, the average 10-m AGL wind speed from the nearest surface observing

[2] Estimating environmental shear from TTU Ka-band radar volume scans was also considered, but most deployments did not conduct a full 360° scan at an angle high enough to find the wind speed and direction at the correct altitudes.

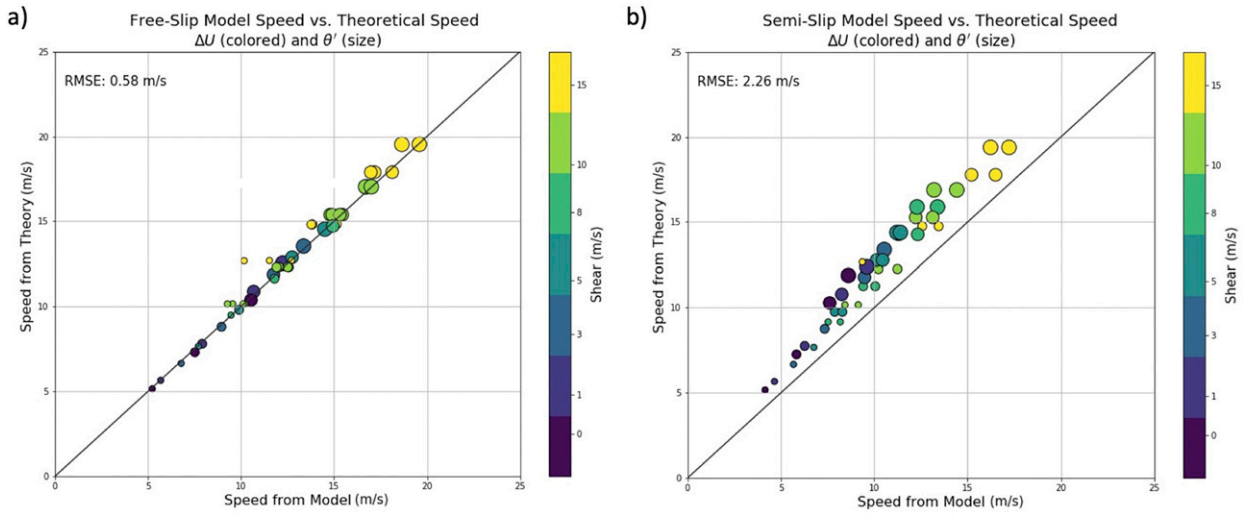

FIG. 4. Cold pool speed from the two-dimensional cold pool model with (a) free-slip and (b) semislip lower boundary conditions vs theoretical cold pool speed calculated from (4) (with ΔU scaled by a factor of 0.5, as discussed in the text). Each point is colored based on the shear used to initialize each simulation. The size of each point represents the thermodynamic deficit initialized within each cold pool (smallest points represent cold pools with $\theta' = 1.5$ K while the largest points represent cold pools with $\theta' = 8.0$ K). The solid line is a 1-to-1 relationship. If theory perfectly predicts the propagation speed of a cold pool in the model, then all the points would fall upon the 1-to-1 line.

platform in each case was substituted into the base of the NEXRAD VAD profile. The shear value used in each case is an average of the shear vectors produced from the VAD and the NARR. The difference between the (adjusted) VAD and NARR is used to estimate the error in the shear profile (the average value of the difference NARR–VAD for the five cases is 1.123 m s^{-1} with a standard deviation of 3.683 m s^{-1}).

Since radar RHIs and two-dimensional cold pool simulations have been employed for this study, it is important to identify the ambient shear in this same two-dimensional plane. To find this two-dimensional vertical shear, the speed of the cold pool in the opposite direction of the scanning (north-relative) azimuth is considered the "cold pool motion vector," and the wind speeds from both the VAD and the NARR are projected into this plane. The ground-relative cold pool motion is then subtracted to create the cold pool–relative wind profile.

3. Results

a. Cold pool propagation speed

Using both the free-slip and semislip lower boundary conditions, cold pool propagation speeds produced by the two-dimensional cold pool model followed the expected trend: cold pools with greater buoyancy deficits moved faster than those with weaker buoyancy deficits. It is also evident that cold pools in stronger shear (10–15 m s^{-1}) moved faster than their counterparts in weaker shear (0–3 m s^{-1}, Fig. 4).

To find an empirical equation for true ground-relative cold pool propagation speed, we develop the following relation:

$$c + \Delta u = \alpha \Delta u + \beta \sqrt{gH \frac{\rho_1 - \rho_0}{\rho_0}} \qquad (4)$$

based on the theoretical equation (2) formulated by Simpson and Britter (1980), where $c + \Delta u$ is the cold pool propagation speed at the surface. The results from the free-slip cold pool model fit best when $\alpha = 0.5$ and $\beta = \sqrt{2}/2$, with a root-mean-square error (RMSE) of 0.58 m s^{-1} (Fig. 4a). As expected, cold pools produced by the semislip model propagate slower than those simulated with free-slip lower boundary conditions (Fig. 4b). Comparing the cold pool speeds predicted by (4) to the cold pool speeds from the semislip model results in an RMSE of 2.26 m s^{-1}. Semislip cold pools move an average of 2 m s^{-1} slower regardless of shear strength or magnitude of cold pool deficit.

To compare observed cold pool speeds with what is produced in the model, ambient shear, cold pool depth, and cold pool buoyancy deficit from each case is input into (4) using the empirical values for α and β calculated from the free-slip model results. It is clear that both the free-slip model and (4) produced very similar cold pool speeds given the same low-level environmental shear (Fig. 4). It was then tested if (4) could predict the cold pool speed that was observed in each of the five field cases (Fig. 5). Observed cold pool speed was calculated with the same method used to find the modeled free-slip

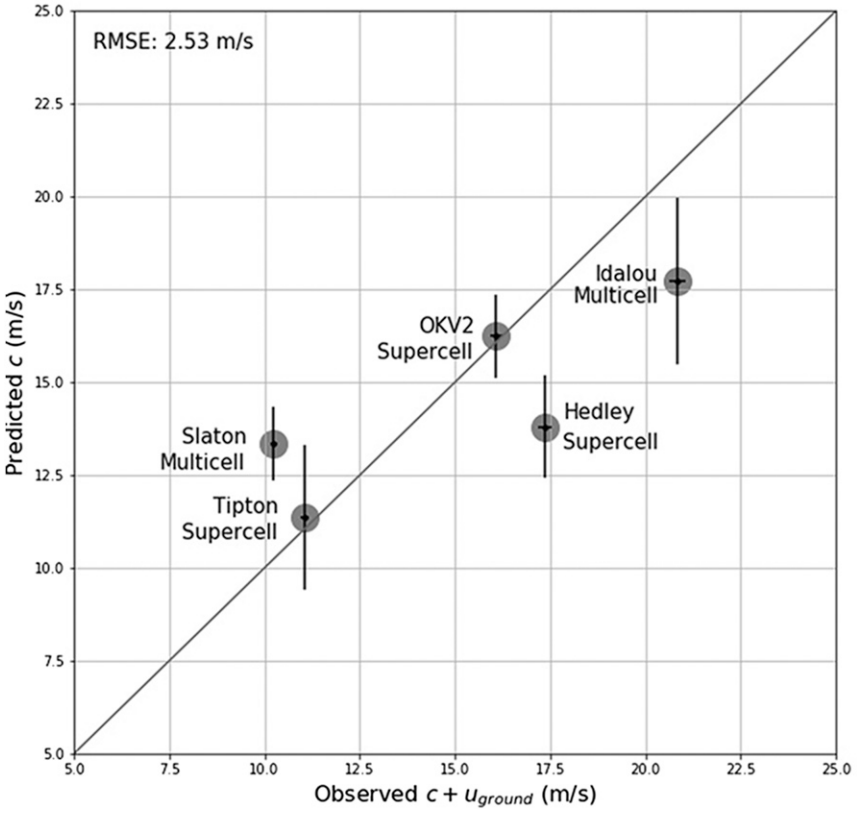

FIG. 5. Scatterplot of c_{obs} vs cold pool speed predicted by (5). Each point is labeled with a name referring to each deployment in which a cold pool was observed along with the distinction between supercell outflow (RFGF) and outflow from upscale multicell storms. The solid line gives a 1-to-1 relationship. Error bars are included along the y axis to indicate the range in speed predicted using both VAD and NARR estimated shear, in addition to the RMSE between modeled speed and speed predicted from (5) (Fig. 4).

cold pool speed (c_{free}), adding the ground-relative observed cold pool propagation (c_{radar}, via Doppler radar velocity plots) to the environmental wind vector measured at the surface out ahead of the cold pool (u_{ground}). With these variables, (4) can be rewritten as

$$c_{radar} - u_{ground} = \frac{1}{2}\Delta u + \sqrt{\frac{1}{2}gH\frac{\rho_1 - \rho_0}{\rho_0}}. \quad (5)$$

For each case, c_{radar} is adjusted to account for the projection of the gust front motion on to the RHI plane.[3] Cold pool speed was predicted from (5) using a shear value averaged between VAD-observed winds and those produced in the NARR over the depth of the observed cold pool (typically over the lowest 1–2 km). An error of 2.37 m s^{-1} was also applied to the speed calculated by (5) to account for the RMSE between modeled and theoretical speed. The model did not show any significant fast or slow bias, so RMSE error bars are centered on each data point.

The observed cold pool speeds are predicted by (5) with an RMSE of 2.53 m s^{-1}. Neither the supercell outflow nor the multicell outflow appear to have either a fast or slow bias (Fig. 5).

To attempt to retrieve the thermodynamic perturbation from cold pool speed, (5) is rearranged to solve for the density excess:

$$\frac{\theta_v^1 - \theta_v^0}{\theta_v^0} = \frac{2\left[(c_{radar} - u_{ground}) - \frac{1}{2}\Delta u\right]^2}{gH}. \quad (6)$$

When this equation is applied to observed thunderstorm outflow (Fig. 6), buoyancy deficits from only two of the five cases are predicted within estimated error. The RMSE is 2.77 K, and the results show that (6) has

[3] In some cases, the radar beam was not scanning directly parallel to the cold pool motion vector. If the scanning angle is ϕ degrees off parallel, only a fraction of the true speed can be observed. The true speed is estimated using $c = c_{radar}/\cos(\phi)$.

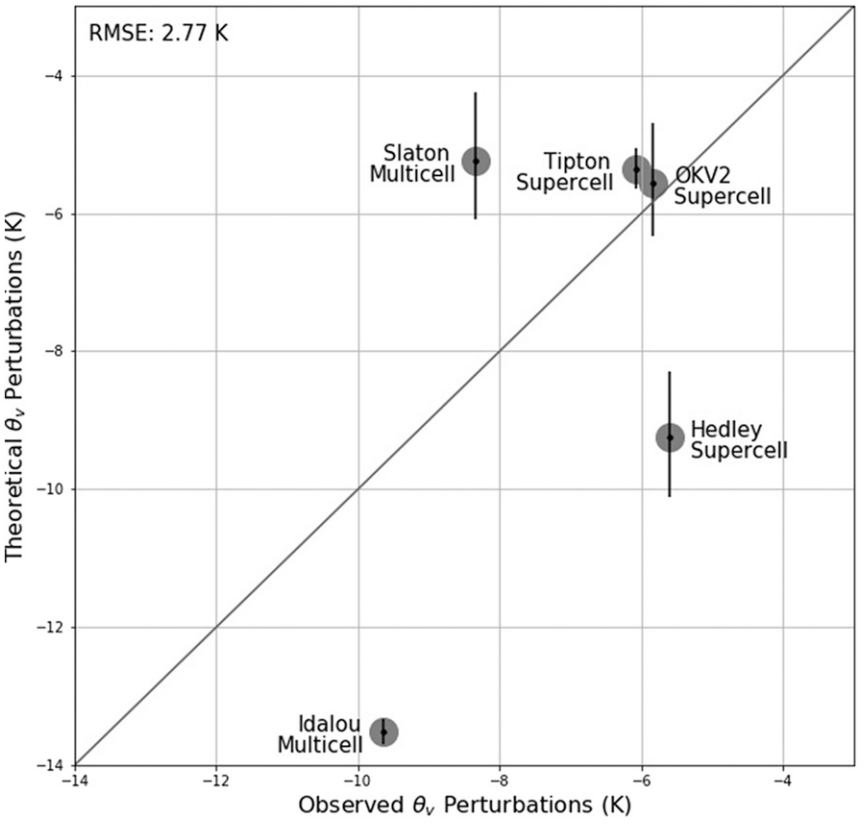

FIG. 6. A scatterplot comparing the derived θ_v perturbations (calculated from observed speed) to the actual observed θ_v perturbations. The error bars along the y axis are calculated using the same method described in Fig. 5.

neither a fast nor a slow bias. It is apparent that predicting buoyancy deficit from cold pool speed is highly sensitive to shear error, with the variance in our shear estimates leading to an average of about 1.6 K in θ_v perturbations.

In this analysis, it is assumed that the cold pool speed and the in situ thermodynamic measurement were observed simultaneously. However, as in situ samples required fortuitous passage of the storm over fixed-site instrumentation, there was often a 20–30 min time difference between the thermodynamic measurement and the cold pool speed and slope measurements (in the Tipton supercell case, the time delay was near 60 min). Unsteady evolution could well have contributed to the buoyancy deficit in the period between when the two measurements were taken. Surges in the RFD, for example, have been shown to be thermodynamically independent of the existing RFD [Marquis et al. (2012) observed such RFD surges in different tornadic supercells]. These surges can be difficult to identify, and by altering the thermodynamic properties of the RFD they can affect the propagation speed of the RFGF.

In spite of some of these challenges, we believe this is a good first step in using radar observations of cold pool speed to estimate cold pool deficit. Due to the estimation's high sensitivity to errors in shear, in situ storm proximity soundings may lead to a greatly improved cold pool deficit estimate. In one case, the VAD/NARR shear approximation was compared to a radiosonde launched in the field an hour before the storm to capture environmental characteristics. The shear vector was found to be very similar across platforms; however, storm proximity soundings can be more sensitive to small increases of shear in near storm environments. Future work is planned to test the utility of improved shear characterization.

b. *Cold pool slope*

1) FREE-SLIP SIMULATION RESULTS

The structure of a cold pool has been shown to largely depend on ambient shear and the depth of the shear layer relative to that of the cold pool (Xu 1992; Chen 1995; Xu et al. 1996; Liu and Moncrieff 1996; Bryan and Rotunno 2014b), and this study aims to show

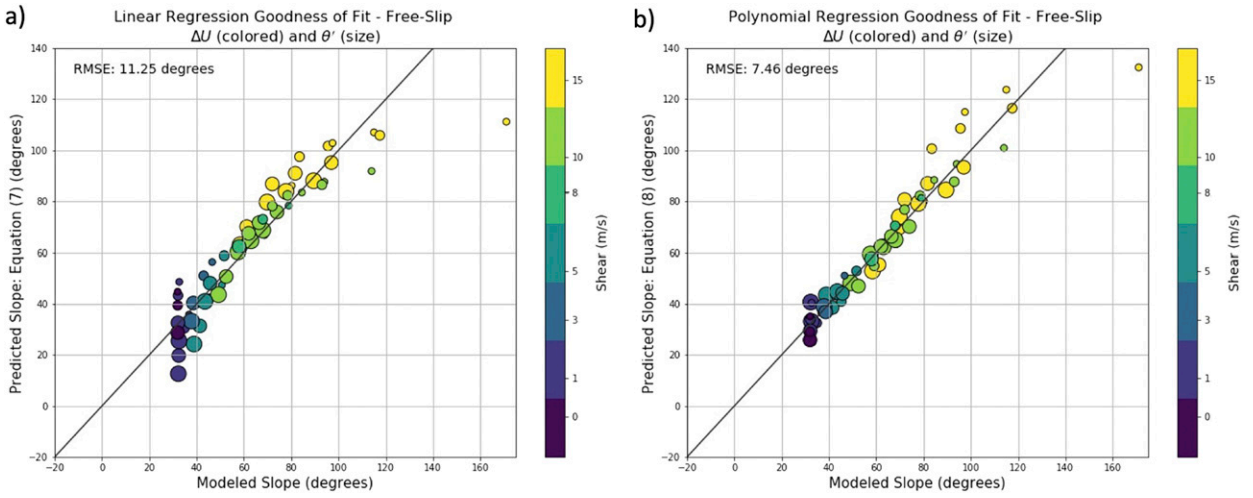

FIG. 7. Scatterplot of cold pool slope from the free-slip model vs the slope predicted from (a) the linear equation (7) and (b) the polynomial equation (8) produced by the multivariate regression analysis on the model data. Each point is colored and sized in the same way as points in Fig. 4. The 1-to-1 relationship is given by the black solid line.

that the magnitude of the buoyancy deficit is also relevant. In an effort to diagnose a cold pool slope given shear (ΔU), shear depth (h/H), and cold pool buoyancy deficit (θ'), a multivariate stepwise regression analysis was conducted on the results from each of the 60 free-slip cold pool model runs to form a linear empirical equation:

$$\text{slope} = 101.48 + 3.64(\Delta U) - 4.26(\theta') - 52.43\left(\frac{h}{H}\right). \quad (7)$$

This equation has an r^2 statistic of 0.830 and an RMSE of 11.25° (a visual representation of how well the linear equation fits the cold pool results can be seen in Fig. 7a). While the ambient shear vector controls a majority of the variance for cold pool slope, it is evident that buoyancy deficit also plays a significant role. The negative coefficient for θ' indicates that weaker (greater) θ deficits are associated with steeper (shallower) slopes. For cold pools in moderate positive shear (5–10 m s^{-1}), the linear regression equation appears to be a relatively good fit for cold pool slope. However, the linear equation does a poor job predicting cold pool slopes in unsheared environments and it does not capture the steep change in slope for weaker cold pools in strong positive shear (e.g., the 1.5 K cold pool slope increases by 50° between the 10 m s^{-1} and 15 m s^{-1} environments, but it only increases by 25° between the 5 and 10 m s^{-1} environments). Due to these limitations of the linear equation, a multivariate nonlinear regression analysis was conducted producing the polynomial equation:

$$\text{slope} = 36.25 - 5.47\left(\frac{h}{H}\right) - 9.43(\theta') + 9.03\left(\theta'\frac{h}{H}\right) + 13.67(\Delta U) - 7.42\left(\Delta U\frac{h}{H}\right) - 0.28(\Delta U\theta') + 0.108(\theta'^2). \quad (8)$$

This equation has an r^2 statistic of 0.931 and an RMSE of 7.46° (Fig. 7b). The second-order terms for θ' and ΔU in the equation are integral to capture the nonlinearity of the model. While the nonlinear regression is a great fit for a majority of the data, and certainly improves cold pool slope prediction in strong positive shear ($\Delta U >$ 10 m s^{-1}) when compared to the linear regression, it appears to have a slight steep bias, although the bias is no greater than 5°.

For cold pools modeled in strong positive shear, the slopes vary by at least 40° over the expanse of θ' values tested, while the cold pools modeled in weak positive shear have slopes that vary over a much smaller range (<20°; Fig. 7b). Those modeled in no shear do not vary at all [which agrees with the theoretical studies for cold pools in the absence of shear, e.g., Benjamin (1968)]. It is clear that the nonlinear equation is more suited to predict cold pool slope given ambient shear and θ' due to the inherent nonlinearity of the results.

2) SEMISLIP SIMULATION RESULTS

Cold pools modeled with the semislip lower boundary condition have steeper slopes to their leading edge than those modeled with a free-slip lower boundary (Fig. 8). The greatest differences in vertical slope occur between cold pools modeled in 15 m s^{-1} ambient shear.

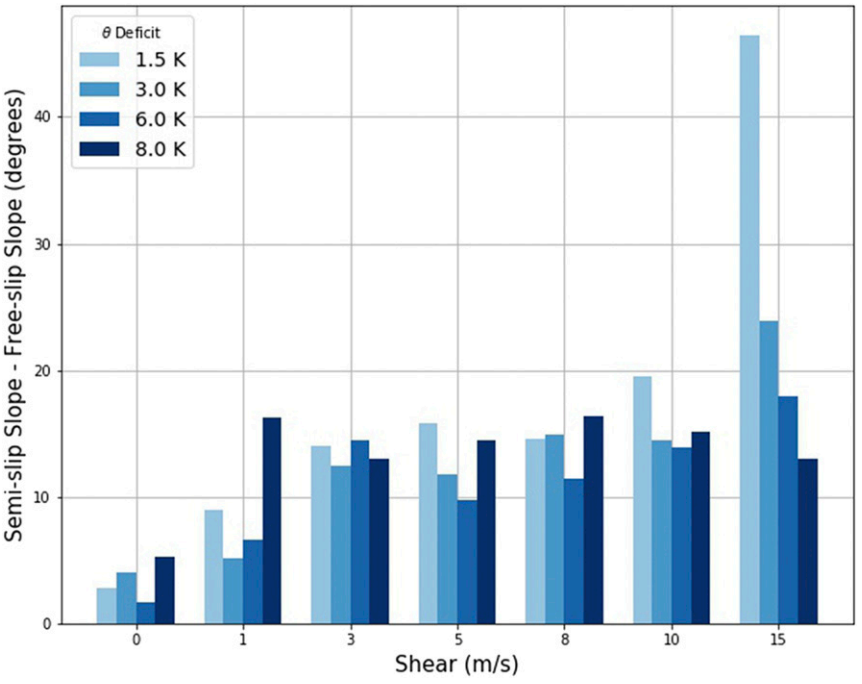

FIG. 8. A bar graph giving the difference in vertical slope between semislip cold pools and free-slip cold pools when simulated with the same potential temperature deficit in the same environmental shear. Results are only given for cold pools in which the shear depth is equal to the cold pool depth (i.e., $h/H = 1$). All differences are positive, indicating that cold pools with a semislip lower boundary condition have a steeper slope than those with a free-slip lower boundary condition.

However, the difference in slopes between the free-slip and semislip cold pools are apparent in cold pools modeled with and without shear (Fig. 9). Comparing snapshots of cold pools in 10 m s^{-1} shear with different lower boundary conditions, we see that the cold air above the surface ($z > 100$ m) bulges ahead of the leading edge at the lowest model level (Figs. 9c,d). While the bulging cold air is not as visible for cold pools modeled in 0 m s^{-1} shear, the semislip cold pool still has a visibly steeper slope than the free-slip cold pool (Figs. 9a,b). The bulging cold air has been referred to as an "elevated nose" (Simpson 1969; Charba 1974), and its appearance in observed cold pools is discussed in a later section.

Semislip cold pool results were analyzed with the same methods used to analyze the free-slip cold pool results. A multivariate stepwise regression analysis was conducted on the results from each of the 44 semislip cold pool model runs to form the linear empirical equation:

$$\text{slope} = 64.10 + 4.24(\Delta U) - 3.14(\theta') - 8.85\left(\frac{h}{H}\right). \quad (9)$$

This equation has an r^2 statistic of 0.860 and an RMSE of 8.54° (Fig. 10a). While the coefficients in (7) and (9) have different magnitudes, the free-slip and semislip cold pools clearly follow the same trend with respect to shear and cold pool deficit. A multivariate nonlinear regression analysis was also conducted to produce the polynomial equation:

$$\text{slope} = 48.44 - 0.03\left(\frac{h}{H}\right) - 7.70(\theta') + 1.27\left(\theta'\frac{h}{H}\right) + 8.80(\Delta U) - 1.70\left(\Delta U\frac{h}{H}\right) - 0.53(\Delta U\theta') + 0.704(\theta'^2). \quad (10)$$

This equation has an r^2 statistic of 0.971 and an RMSE of 3.84° (Fig. 10b). Both nonlinear polynomials are used to determine how well observed cold pools match the two-dimensional cold pool model.

3) OBSERVED SLOPE VERSUS MODELED SLOPE

Observed cold pool slopes were compared to slopes produced by the model by inputting observed buoyancy deficits and shear from each of the five cases into both the free-slip nonlinear regression in (8) (Fig. 7b) and the semislip nonlinear regression (10) (Fig. 10b). The shear used to predict the slope for each case is averaged between the (adjusted) value observed from the nearest WSR-88D VAD and that analyzed in the NARR, with error bars covering the range between the two sources.

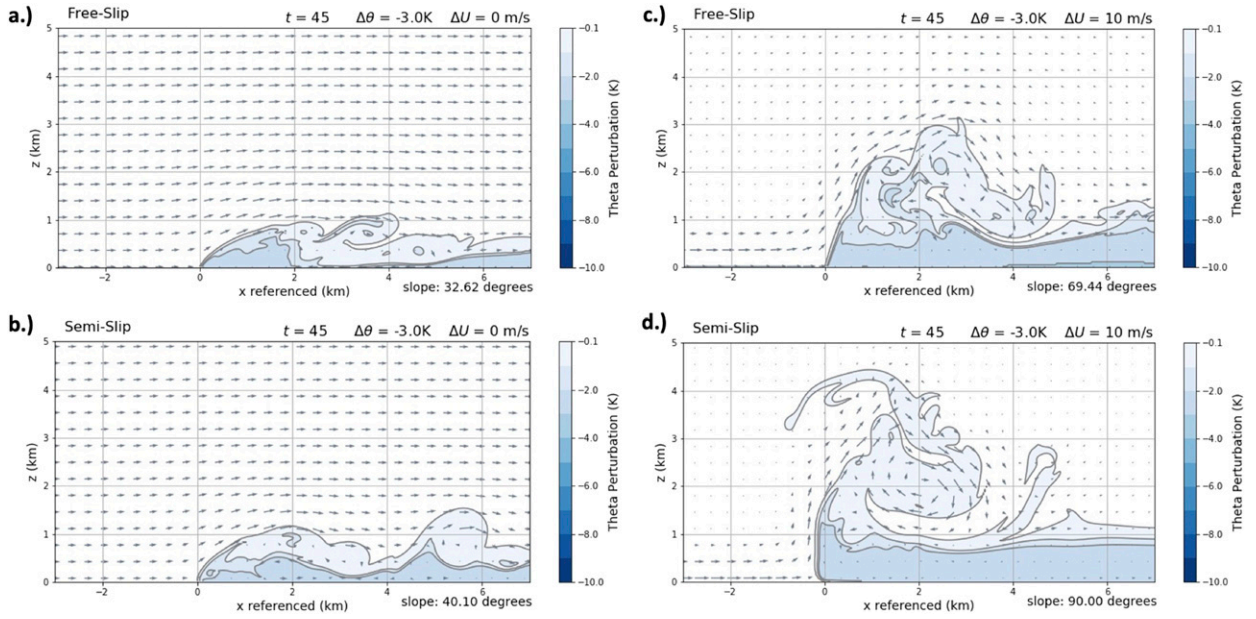

FIG. 9. Cross-sectional plots of potential temperature deficit for 3 K cold pools modeled with (a) the free-slip lower boundary and 0 m s^{-1} shear, (b) the semislip lower boundary and 0 m s^{-1} shear, (c) the free-slip lower boundary condition and 10 m s^{-1} shear, and (d) the semislip lower boundary and 10 m s^{-1} shear. All wind vectors are relative to cold pool motion.

Neither the free-slip model nor the semislip model accurately predicts the cold pool slopes in our small sample of observed cases (Fig. 11). The free-slip nonlinear regression (Fig. 11a) underpredicts the three supercell cold pools and overpredicts the two multicell cold pools, and no slope is predicted within the estimated error. The semislip nonlinear regression (Fig. 11b) mainly underpredicts all cold pool slopes, but does capture the Slaton Multicell cold pool slope within estimated error. More observed cold pool cases are necessary–particularly with representative proximity soundings immediately ahead of the gust front–to properly assess how well the model predicts the slope of observed gust fronts.

4) OTHER STRUCTURAL SIMILARITIES

To directly compare the structure of modeled cold pools to those observed with mobile radars, simulated Doppler radar RHIs were produced from the model data. While the vertical slope of observed cold pools did not exactly match with what was predicted by the model, the two-dimensional simulations did produce cold pools with characteristics similar to those seen in observed

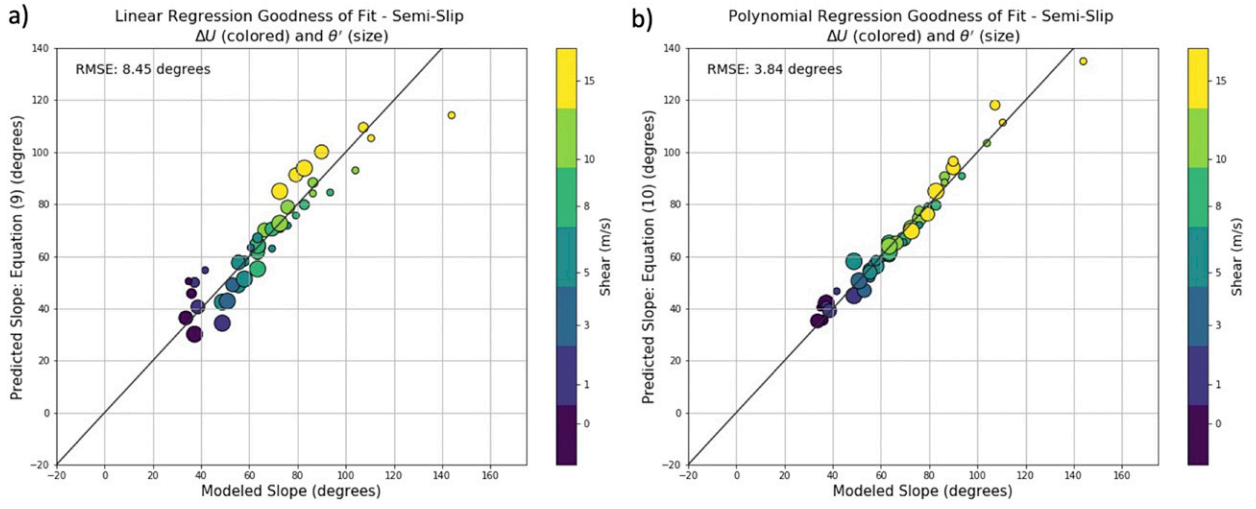

FIG. 10. As in Fig. 7, but for semislip lower boundary conditions.

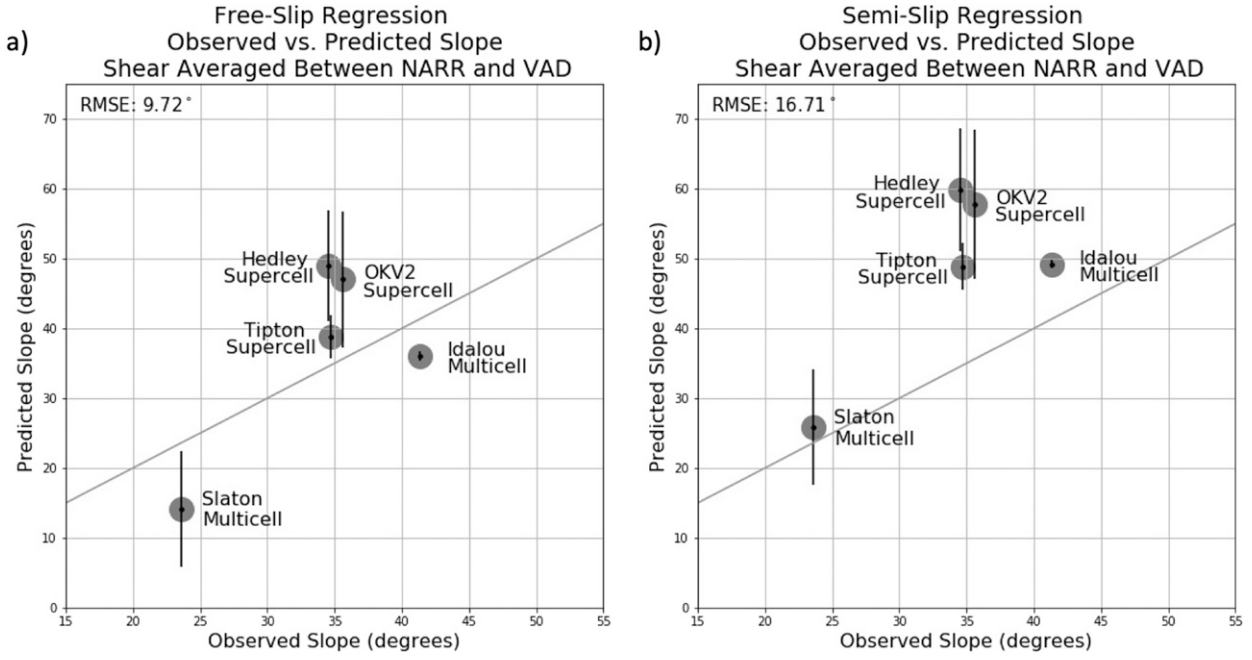

FIG. 11. Scatterplots comparing observed slopes to the slopes predicted by (a) the nonlinear free-slip regression (8) and (b) the nonlinear semislip regression (10). The slopes are plotted relative to a gray line that provides the 1-to-1 relationship between observed slope and model predicted slope. Model slopes are predicted using the average shear value between observed VAD winds and analyzed NARR winds. Error bars cover the difference between the two shear estimates.

cold pools. One such feature is an internal rotor near the surface and about 1 km behind the leading edge of the cold pool (Figs. 12a,c). The rotor is visible as a small patch of outbound velocities at the surface embedded within the inbound velocities that signify the cold pool. While the rotor appears in only one observed cold pool (behind the Hedley RFGF; Fig. 12a, although the outflow from the Idalou multicell system exhibits a decrease in inbound velocities along the surface in the same location; Fig. 12b), it can be seen in several of the modeled cold pools (e.g., Fig. 12c). This near-surface rotor is the result of two larger eddies on the upper boundary of the cold pool penetrating at least halfway into the body of the cold pool (visible through the wind vectors plotted in Fig. 12d). The two eddies then cause the cold air near the surface to overturn and rotate in the opposite direction, with a jet of enhanced wind speeds in the region between upper eddies and the eddy near the surface. Bryan and Rotunno (2014a) show that such eddies are especially exaggerated in two-dimensional simulations, which may explain why the surface rotors are more common in our simulations than in the observations. However, further research is needed to understand under what circumstances this rotor forms in our observations and if it can reveal any information about the cold pool or ambient environment.

Another result from the two-dimensional simulated Doppler velocity plots is that all of the cold pools visibly lack an elevated nose. A number of prior studies (e.g., Simpson 1969; Charba 1974) that involve observations and laboratory experiments often refer to an elevated (500–750 m AGL) region of the cold pool that juts out past the cold air at the surface. None of the cold pools observed by the authors using the TTU Ka-band mobile Doppler radar in this study have a visible elevated nose (e.g., Figs. 12a,b). In the semislip simulation, cold pools are characterized by a small, very shallow (200 m AGL) elevated nose (e.g., Fig. 12d). However, the nose is not visible in the simulated two-dimensional wind field (Fig. 12c), which may be the result of a small area of nonhydrostatic high pressure extends out ahead of the gust front, consistent with the decceleration of outbound environmental flow ahead of the gust front passage (Bryan and Rotunno 2014b). Therefore, the zero isodop extends farther ahead of the edge of cold air along the surface in the simulated two-dimensional wind field (Fig. 12c).

5) VORTICITY BUDGET ANALYSIS

In an effort to more deeply understand the mechanisms driving the change in cold pool slope with varying shear and cold pool strength, the vorticity budget near the leading edge of the cold pool is analyzed. Following the vorticity budget analysis (3) conducted by Bryan and Rotunno (2014b), the vorticity flux is measured at the

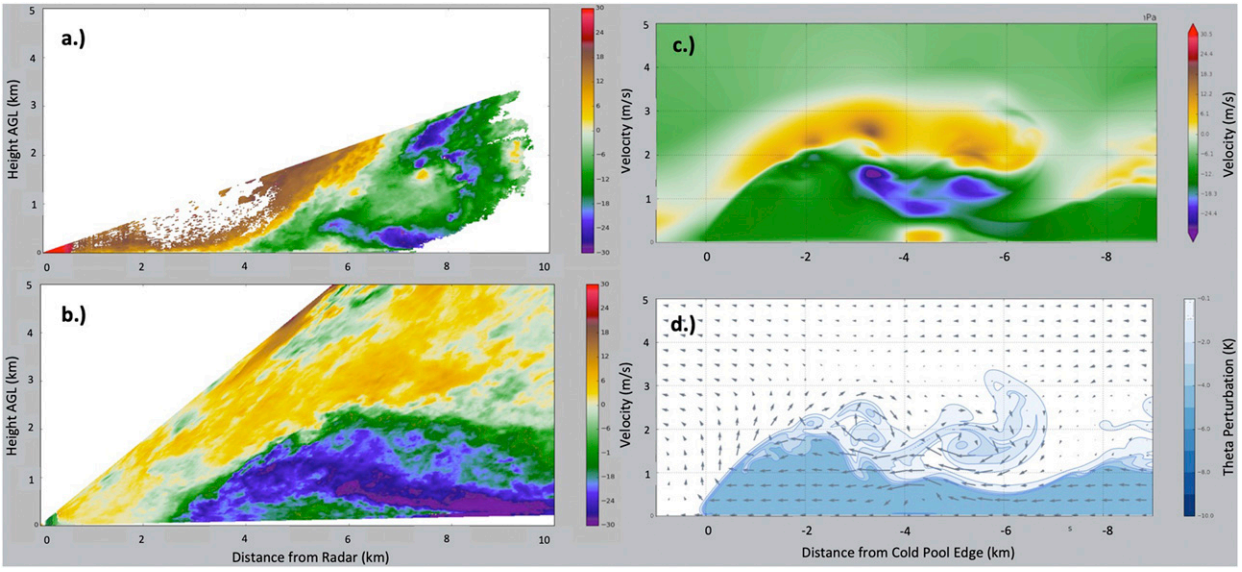

FIG. 12. Doppler base velocity RHIs from the Ka-band mobile radar revealing the vertical structure of (a) the RFGF from a tornadic supercell in Hedley, TX, on 15 May 2015 and (b) the outflow of a severe mesoscale convective system in Idalou, TX, on 15 Jun 2016. (c) A simulated Doppler velocity plot of a 5 K deficit cold pool from the two-dimensional model (only horizontal wind is color filled). (d) A plot of the same cold pool at the same time as shown in (c), but potential temperature deficit is contoured and color filled along with two-dimensional ground-relative wind barbs.

top, left, and right boundaries of a CV centered on the leading edge of the cold pool. Each boundary is located 2 km from the cold pool edge. The net generation of vorticity is also measured within the CV, as well as the overall tendency (i.e., the total change in vorticity) within the CV.[4] The vorticity analysis is conducted only for free-slip cold pools, in order to follow the analysis of Bryan and Rotunno (2014b) as well as to gain an understanding of vorticity tendencies without the added influence of a semislip lower boundary.

First, the vorticity budget is analyzed over several cold pools with different initial potential temperature deficits in 15 m s^{-1} ambient shear (Fig. 13). The cold pool with a 1.5 K θ-deficit has an average slope of about 98° (past vertical), the cold pool with a 3 K deficit has an average slope of about 84° (near vertical), and the cold pool with a 6 K deficit has an average slope of about 72° (under vertical; Fig. 13). We first look at the vorticity budget of the cold pool closest to RKW88's optimal state: the 3 K cold pool.

Throughout the lifetime of the 3 K cold pool, the largest terms in the vorticity budget equation are the flux-at-right and net-generation terms (Figs. 14c,d). These results match nearly identically with Bryan and Rotunno (2014b) optimal state vorticity budget. The ambient shear creates a positive flux of vorticity on the right side of the CV, while the baroclinic generation of negative vorticity by the cold pool (i.e., the net-generation term) is nearly equal but opposite of the flux-at-right term, resulting in a nearly vertical gust front slope (as shown in Fig. 13b).

The flux-at-top and tendency terms for the 3.0 K cold pool are constantly fluctuating within the CV, but their average values are relatively low (Fig. 14d). RKW88 assume these terms to be zero in the optimal state, while Bryan and Rotunno (2014b) show that these terms do average out to be nearly zero. The results shown in this paper match the results presented by Bryan and Rotunno (2014b), so we can make conclusions from the vorticity budget analysis with confidence as we move forward.

The 1.5 K cold pool and 6 K cold pool are both in "nonoptimal" states, where the net-generation of baroclinic vorticity and the horizontal vorticity due to ambient shear are out of balance (Figs. 13a,c). Because the 1.5 K cold pool has a slope past vertical, we can assume that the shear vorticity (i.e., the flux at right term) is stronger than the generation of baroclinic vorticity. However, Fig. 14a implies that the flux-at-right term is actually weaker than the baroclinic vorticity (and weaker than what is expected to be produced by 15 m s^{-1}

[4] While specific residuals can be somewhat large, the average residual is negligibly small. Bryan and Rotunno (2014b) attribute these fluctuations to viscous terms that have not been considered in this analysis.

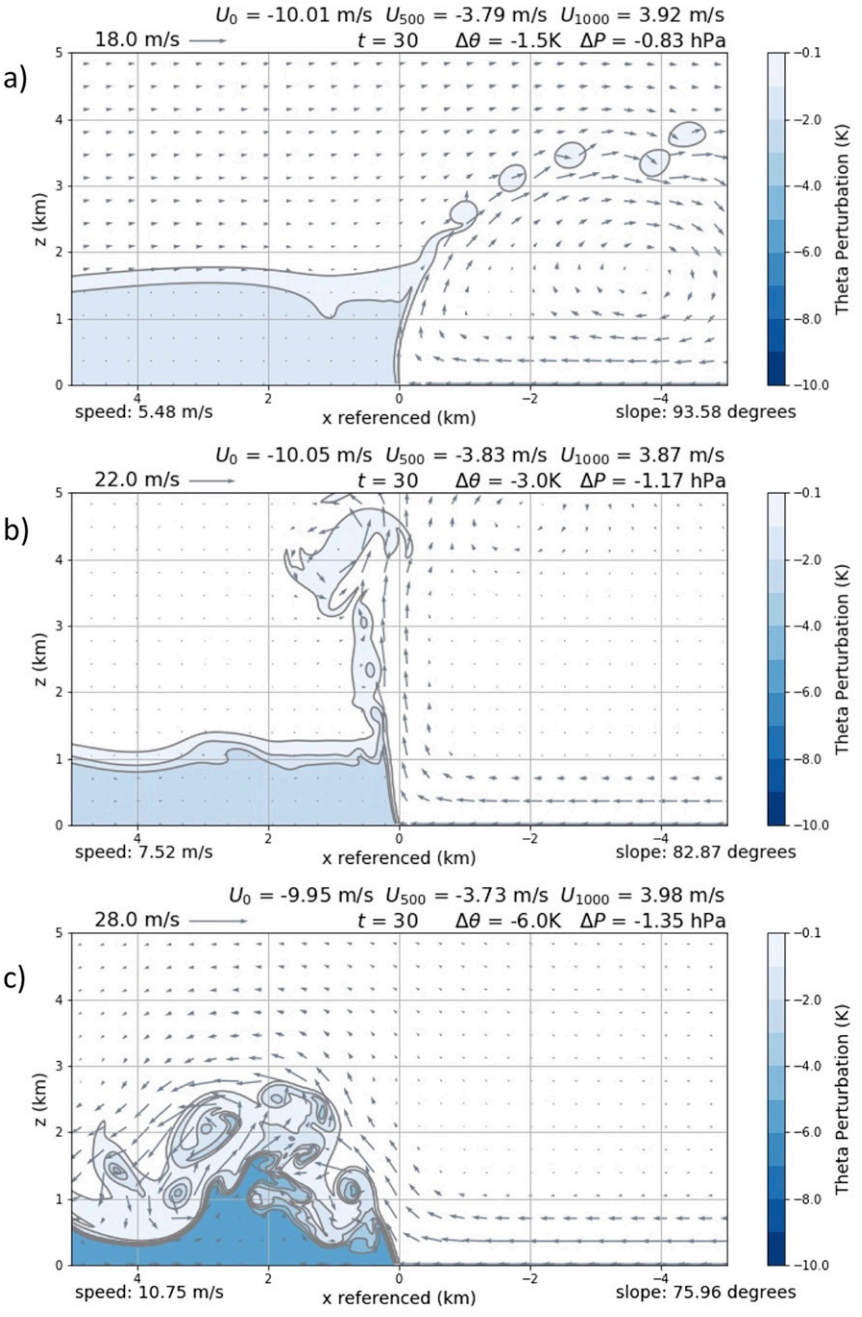

FIG. 13. Free-slip cold pool model output for a (a) 1.5 K cold pool deficit, (b) 3.0 K cold pool deficit, and (c) 6.0 K cold pool deficit in 15 m s^{-1} ambient shear at the model time of 30 min. Potential temperature deficit is contoured and color filled and wind vectors represent cold pool–relative flow.

shear). Looking at a snapshot of the simulated cold pool (Fig. 13a), it is clear that the reason for the weak flux-at-right term is because the positive vorticity injected into the CV by the ambient shear is negated by the advection of negative baroclinic vorticity out the right side of the CV, therefore decreasing the net value of the term.

The 6 K cold pool has a slope that is under vertical, consistent with baroclinic generation of vorticity that is greater that the ambient shear vorticity (Figs. 13c and 14e). The turbulent eddies produced along the cold pool interface cause large fluctuations of both the flux-at-left and net-generation terms within the CV over time, but

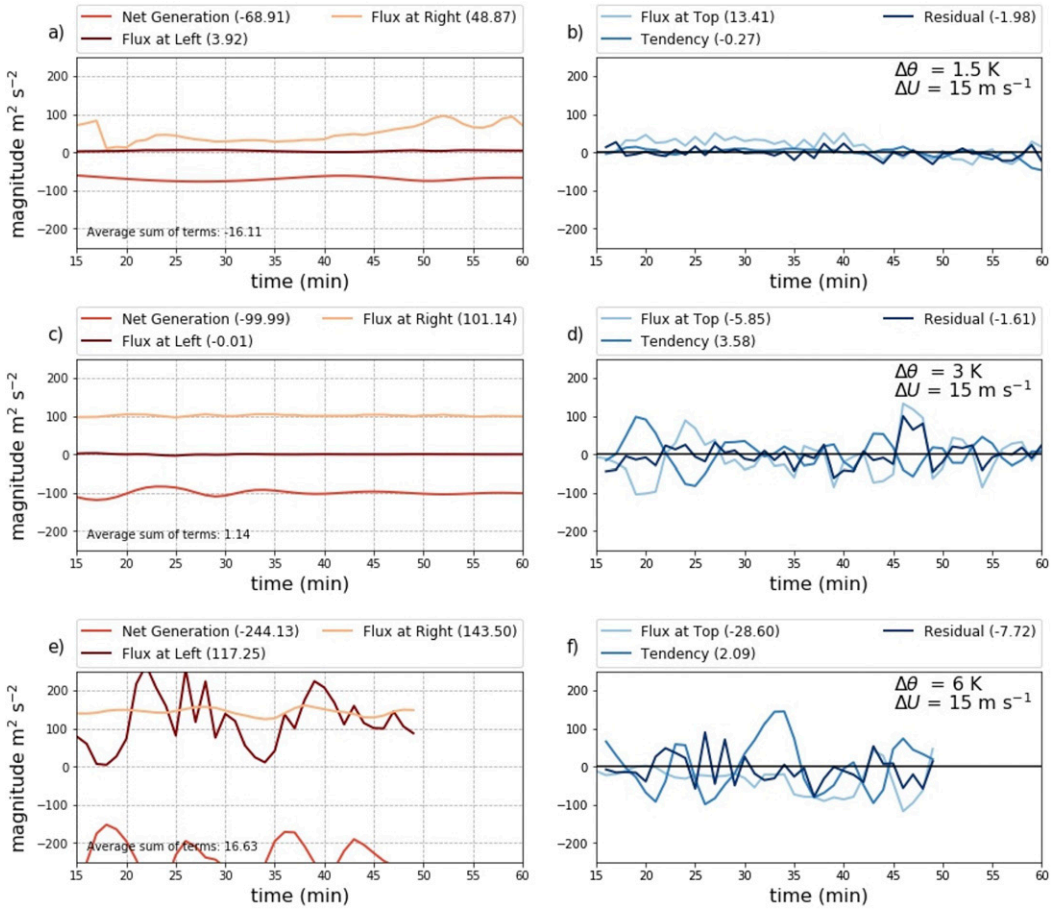

FIG. 14. Time evolution of the horizontal vorticity budget for a (a),(b) 1.5 K cold pool deficit, (c),(d) 3.0 K cold pool deficit, and (e),(f) 6.0 K cold pool deficit in 15 m s^{-1} ambient shear. Each line (as indicated by the legend) corresponds to a term in (3). The average value of each term over the time period is given in parentheses in the legend.

the average values of the flux-at-right and net-generation terms reveal that the stronger cold pool in 15 m s^{-1} shear produces greater vorticity than the ambient shear.

Next, the vorticity budget is analyzed over different cold pools in an environment with no ambient shear. As hypothesized by RKW88, all cold pools in an unsheared environment have the same vertical slope, regardless of cold pool deficit (Fig. 15). It is apparent from the vorticity budget analysis (Fig. 16) that the average baroclinic vorticity generated by the cold pool is nearly equal (but opposite to) the flux of vorticity out the left side of the domain (while the remaining terms are zero or negligible). These results support the claim made by RKW88 (p. 478), that without the injection of vorticity over the right boundary due to shear, "the net buoyant generation of negative vorticity is just balanced by the export of negative vorticity" out the left side of the CV. This statement suggests that any baroclinic vorticity generated by a cold pool of any strength does not remain resident in the domain. In the 2D cold pool simulations conducted in this study, every cold pool simulated in a no-shear environment ended up having the same slope (about 32°).

Since the CV follows the leading edge of the cold pool, the faster propagation for stronger cold pools in the no-shear environment leads to a greater flux of vorticity over the left side of the domain, balancing the greater baroclinic tendency. Without any ambient shear injecting vorticity into the CV, the vorticity budget remains balanced and the potential temperature deficit of the cold pool does not affect its slope. When ambient shear is introduced into the domain, the positive shear combats the downwind advection of the baroclinic vorticity and advects it instead in a more upward trajectory. This in turn allows the cold pool to retain a greater depth, increasing the generation of baroclinic vorticity (e.g., Fig. 14), all while retaining positive vorticity previously generated within the domain. The crucial point is that cold pools with varying buoyancy deficits generate

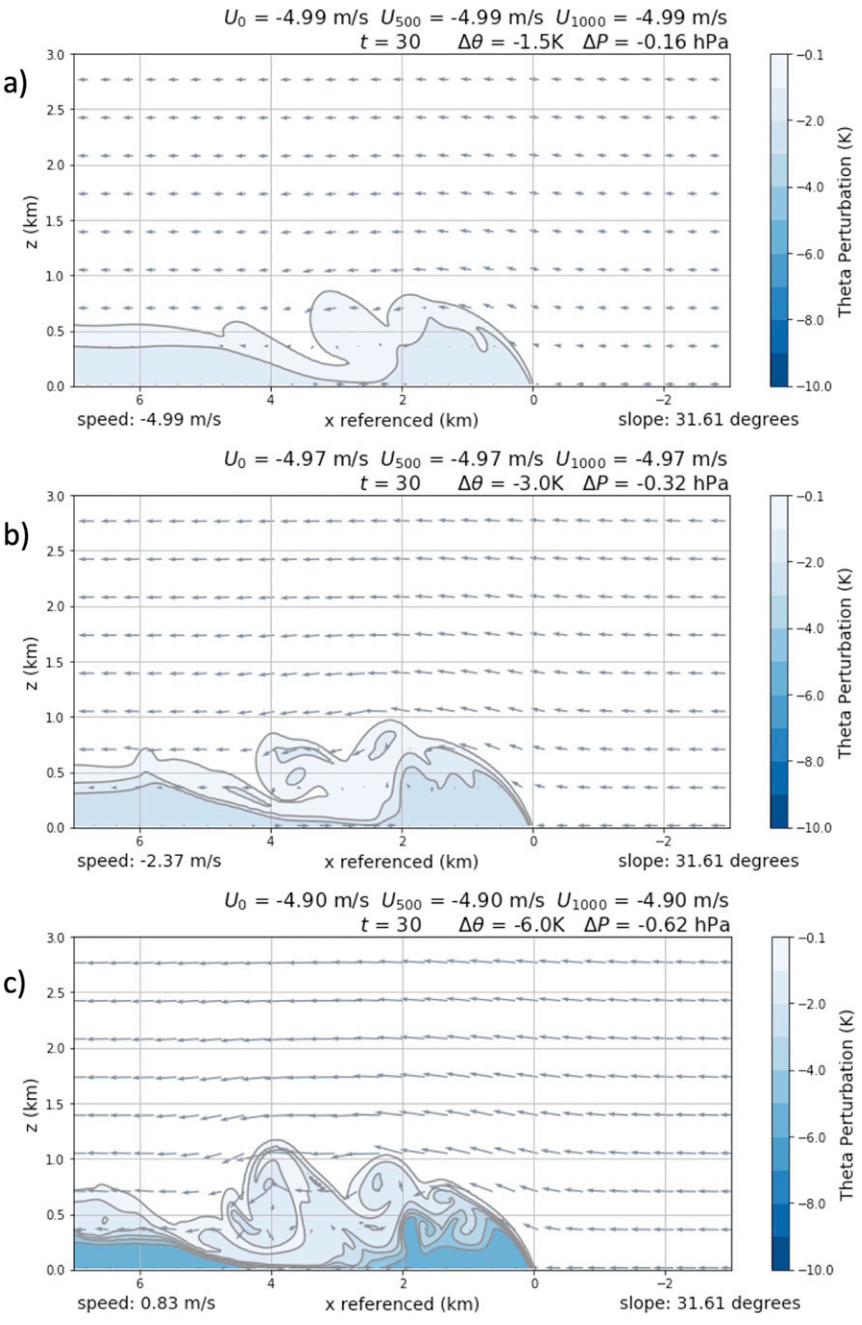

FIG. 15. As in Fig. 13, but for cold pools in an environment with no ambient shear.

different amounts of baroclinic vorticity that, when interacting with positive vorticity injected by ambient shear, affect the cold pool slope.

4. Summary and conclusions

Previous studies have shown that stronger tornadic storms are associated with warmer outflow, while strong buoyancy deficits were measured within the RFDs of weakly tornadic or nontornadic supercells (Markowski 2002; Markowski et al. 2002; Grzych et al. 2007; Hirth et al. 2008; Finley and Lee 2008; Markowski and Richardson 2009; Weiss et al. 2015). With this motivation in mind, the purpose of this study is to determine how internal buoyancy deficits affect the vertical structure and propagation of thunderstorm outflow (like the RFGF) and if those differences can be observed using a Ka-band mobile Doppler radar.

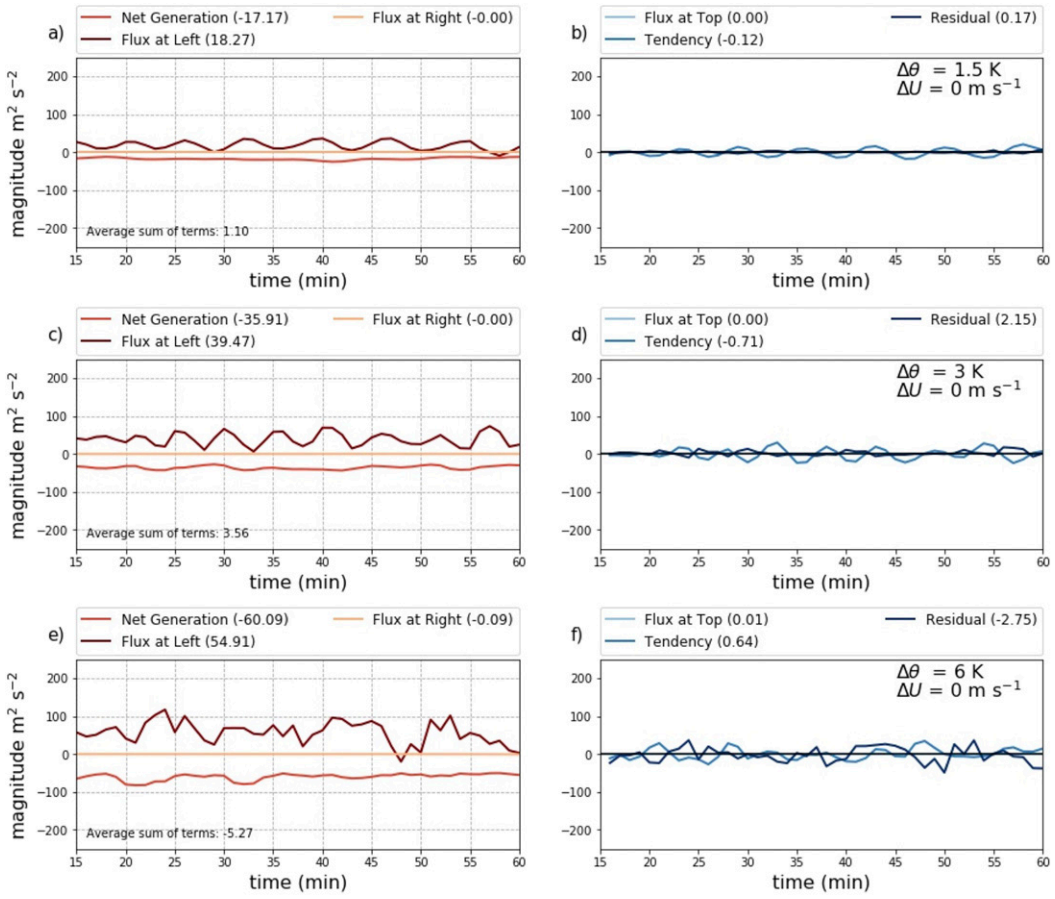

FIG. 16. As in Fig. 14, but for cold pools in an environment with no ambient shear.

A two-dimensional cold pool model introduced in Bryan and Rotunno (2014b) was used to analyze how the vertical structure and propagation of a cold pool evolves with changing potential temperature deficit, ambient shear, and shear depth. While the original model only operated with a free-slip lower boundary, a semislip lower boundary was also introduced in the current study. The resultant propagation speed and leading edge slope of each simulated cold pool were then compared to speeds and slopes of five different gust fronts observed using the Texas Tech Ka-band mobile Doppler radar.

In both the free-slip and semislip models, as expected, cold pools initialized with greater potential temperature deficits propagated faster. For cold pools with the same thermodynamic characteristics, the model showed that stronger ambient shear increased cold pool propagation speed. It was found that the cold pool propagation speeds from the free-slip model correlate strongly with the relation shown in (4) based off of the original empirical equation from Simpson and Britter (1980). The propagation speed for cold pools simulated with a semislip lower boundary follow the same trend as (4), but, as expected, the average propagation speed was about 3–5 $m\,s^{-1}$ slower than those in the free-slip model.

Three out of the five observed cold pool propagation speeds were predicted within error by (5). However, the method of quantifying ambient shear caused uncertainty in predicted speed up to 5 $m\,s^{-1}$, which leads to a maximum error in estimated cold pool θ_v deficit of about 3 K. Only two of the five observed cold pool buoyancy deficits were estimated within acceptable error. It seems likely that a more accurate measurement of ambient shear would have better predicted the cold pool buoyancy deficit in our cases.

The dependence of the gust front slope on the buoyancy deficit and ambient low-level shear was similarly tested. Unlike cold pool propagation speed, to the authors' knowledge, there is no analytical equation for the slope that relates these parameters. Using the results from 58 different cold pool simulations with a free-slip lower boundary we developed linear and nonlinear empirical relationships for cold pool slope given ambient

shear, shear depth, and potential temperature deficit [see (7) and (8)]. We also used results from 43 different simulations with a semislip lower boundary to develop similar equations for cold pool slopes in an environment with surface friction [see (9) and (10)].

Both linear multivariate regression equations were a good fit for cold pools in moderate positive shear (i.e., $5 < \Delta U < 10\,\mathrm{m\,s^{-1}}$). The greatest factor in determining cold pool slope is ambient low-level shear, which corresponds with previous studies (e.g., RKW88; Xu et al. 1996). It is also evident that cold pool buoyancy deficit explains much of the remaining slope variance for both the free-slip and semislip models, whereby warmer (colder) cold pools have greater (shallower) slopes when shear is positive. Cold pools with strong buoyancy deficits generate a large amount of baroclinic vorticity that is greater in magnitude than the environmental vorticity from ambient shear, leading to a shallower slope. However, buoyancy deficit has no effect on cold pool slope when in unsheared flow, and it is apparent that the linear equations could not capture the trend of cold pool slopes in no shear or strong positive shear. For this reason, a nonlinear multivariate regression equation was produced from both the free-slip and semislip data. For both models, the nonlinear regressions had the highest correlations with the model slope data when buoyancy deficit was treated as second-order variable, and shear depth as a first-order variable. Both nonlinear equations improved over their linear counterparts, especially for cold pools in unsheared flow and strong positive shear.

Cold pools simulated with the semislip model had steeper slopes than the same cold pools simulated with the free-slip lower boundary condition. Neither the free-slip model nor the semislip model were very accurate in producing the cold pool slopes observed in the five mobile radar intercepts, though there may be some indication that the trend of the slope is captured in our small sample size.

It is apparent that cold pool slope is sensitive to small variations in shear. Though these estimates were the best available for the identified cases, it is known that thunderstorms, especially supercells, feature strong local dynamic accelerations that create significant spatial heterogeneity and temporal evolution of the low-level vertical wind shear. Relatively distant VADs from WSR-88Ds cannot measure such short-term changes, and NARR soundings do not resolve low-level inflow details as well as desired. For future work, it will be important to measure the near-storm shear with either VADs from a mobile radar or in situ soundings to better validate the methods described in this paper.

Acknowledgments. This work was supported by NSF Grants IIS-1527183 and AGS-1824713. We would like to acknowledge support from the High Performance Computing Center at Texas Tech University. We thank the first author's committee members, Dr. Eric Bruning and Dr. Johannes Dahl for providing helpful feedback to improve this research. We would also like to thank the editor and anonymous reviewers for their thorough review that improved this manuscript.

REFERENCES

Adlerman, E. J., K. K. Droegemeier, R. Davies-Jones, E. J. Adlerman, K. K. Droegemeier, and R. Davies-Jones, 1999: A numerical simulation of cyclic mesocyclogenesis. *J. Atmos. Sci.*, **56**, 2045–2069, https://doi.org/10.1175/1520-0469(1999)056<2045:ANSOCM>2.0.CO;2.

Beck, J., and C. Weiss, 2013: An assessment of low-level baroclinity and vorticity within a simulated supercell. *Mon. Wea. Rev.*, **141**, 649–669, https://doi.org/10.1175/MWR-D-11-00115.1.

——, J. L. Schroeder, and J. M. Wurman, 2006: High-resolution dual-Doppler analyses of the 29 May 2001 Kress, Texas, cyclic supercell. *Mon. Wea. Rev.*, **134**, 3125–3148, https://doi.org/10.1175/MWR3246.1.

Benjamin, T. B., 1968: Gravity currents and related phenomena. *J. Fluid Mech.*, **31**, 209–248, https://doi.org/10.1017/S0022112068000133.

Bluestein, H. B., 2013: *Severe Convective Storms and Tornadoes: Observations and Dynamics*. Praxis/Springer, 456 pp.

Bolton, D., 1980: The computation of equivalent potential temperature. *Mon. Wea. Rev.*, **108**, 1046–1053, https://doi.org/10.1175/1520-0493(1980)108<1046:TCOEPT>2.0.CO;2.

Brock, F. V., K. C. Crawford, R. L. Elliott, G. W. Cuperus, S. J. Stadler, H. L. Johnson, and M. D. Eilts, 1995: The Oklahoma Mesonet: A technical overview. *J. Atmos. Oceanic Technol.*, **12**, 5–19, https://doi.org/10.1175/1520-0426(1995)012<0005:TOMATO>2.0.CO;2.

Bryan, G. H., and J. M. Fritsch, 2002: A benchmark simulation for moist nonhydrostatic numerical models. *Mon. Wea. Rev.*, **130**, 2917–2928, https://doi.org/10.1175/1520-0493(2002)130<2917:ABSFMN>2.0.CO;2.

——, and R. Rotunno, 2014a: Gravity currents in confined channels with environmental shear. *J. Atmos. Sci.*, **71**, 1121–1142, https://doi.org/10.1175/JAS-D-13-0157.1.

——, and ——, 2014b: The optimal state for gravity currents in shear. *J. Atmos. Sci.*, **71**, 448–468, https://doi.org/10.1175/JAS-D-13-0156.1.

Charba, J., 1974: Application of gravity current model to analysis of squall-line gust front. *Mon. Wea. Rev.*, **102**, 140–156, https://doi.org/10.1175/1520-0493(1974)102<0140:AOGCMT>2.0.CO;2.

Chen, C., 1995: Numerical simulations of gravity currents in uniform shear flows. *Mon. Wea. Rev.*, **123**, 3240–3253, https://doi.org/10.1175/1520-0493(1995)123<3240:NSOGCI>2.0.CO;2.

Davies-Jones, R., 1982: A new look at the vorticity equation with application to tornadogenesis. Preprints, *12th Conf. on Severe Local Storms*, San Antonio, TX, Amer. Meteor. Soc., 249–252.

——, and H. E. Brooks, 1993: Mesocyclongenesis from a theoretical perspective. *Tornadoes and Tornadic Storms: A Review of Conceptual Models*, *Geophys. Monogr.*, Vol. 79, Amer. Geophys. Union, 105–114.

——, R. J. Trapp, and H. B. Bluestein, 2001: Tornadoes and tornadic storms. *Severe Convective Storms, Meteor. Monogr.*, No. 50, Amer. Meteor. Soc., 167–221, https://doi.org/10.1175/0065-9401-28.50.167.

Dowell, D. C., and H. B. Bluestein, 1997: The Arcadia, Oklahoma, storm of 17 May 1981: Analysis of a supercell during tornadogenesis. *Mon. Wea. Rev.*, **125**, 2562–2582, https://doi.org/10.1175/1520-0493(1997)125<2562:TAOSOM>2.0.CO;2.

Finley, C. A., and B. D. Lee, 2008: Mobile mesonet observations of an intense RFD and multiple RFD gust fronts in the May 23 Quinter, Kansas tornadic supercell during TWISTEX 2008. *24th Conf. on Severe Local Storms*, Savannah, GA, Amer. Meteor. Soc., P3.18, https://ams.confex.com/ams/24SLS/techprogram/paper_142133.htm.

Grzych, M. L., B. D. Lee, and C. A. Finley, 2007: Thermodynamic analysis of supercell rear-flank downdrafts from Project ANSWERS. *Mon. Wea. Rev.*, **135**, 240–246, https://doi.org/10.1175/MWR3288.1.

Gunter, W. S., J. L. Schroeder, and B. D. Hirth, 2015: Validation of dual-Doppler wind profiles with in situ anemometry. *J. Atmos. Oceanic Technol.*, **32**, 943–960, https://doi.org/10.1175/JTECH-D-14-00181.1.

Hirth, B. D., J. L. Schroeder, and C. C. Weiss, 2008: Surface analysis of the rear-flank downdraft outflow in two tornadic supercells. *Mon. Wea. Rev.*, **136**, 2344–2363, https://doi.org/10.1175/2007MWR2285.1.

Klemp, J. B., and R. Rotunno, 1983: A study of the tornadic region within a supercell thunderstorm. *J. Atmos. Sci.*, **40**, 359–377, https://doi.org/10.1175/1520-0469(1983)040<0359:ASOTTR>2.0.CO;2.

——, R. B. Wilhelmson, and P. S. Ray, 1981: Observed and numerically simulated structure of a mature supercell thunderstorm. *J. Atmos. Sci.*, **38**, 1558–1580, https://doi.org/10.1175/1520-0469(1981)038<1558:OANSSO>2.0.CO;2.

Lemon, L. R., and C. A. Doswell, 1979: Severe thunderstorm evolution and mesocyclone structure as related to tornadogenesis. *Mon. Wea. Rev.*, **107**, 1184–1197, https://doi.org/10.1175/1520-0493(1979)107<1184:STEAMS>2.0.CO;2.

Liu, C., and M. W. Moncrieff, 1996: A numerical study of the effects of ambient flow and shear on density currents. *Mon. Wea. Rev.*, **124**, 2282–2303, https://doi.org/10.1175/1520-0493(1996)124<2282:ANSOTE>2.0.CO;2.

Markowski, P. M., 2002: Hook echoes and rear-flank downdrafts: A review. *Mon. Wea. Rev.*, **130**, 852–876, https://doi.org/10.1175/1520-0493(2002)130<0852:HEARFD>2.0.CO;2.

——, 2016: An idealized numerical simulation investigation of the effects of surface drag on the development of near-surface vertical vorticity in supercell thunderstorms. *J. Atmos. Sci.*, **73**, 4349–4385, https://doi.org/10.1175/JAS-D-16-0150.1.

——, and Y. P. Richardson, 2009: Tornadogenesis: Our current understanding, forecasting considerations, and questions to guide future research. *Atmos. Res.*, **93**, 3–10, https://doi.org/10.1016/j.atmosres.2008.09.015.

——, and ——, 2014: The influence of environmental low-level shear and cold pools on tornadogenesis: Insights from idealized simulations. *J. Atmos. Sci.*, **71**, 243–275, https://doi.org/10.1175/JAS-D-13-0159.1.

——, J. M. Straka, and E. N. Rasmussen, 2002: Direct surface thermodynamic observations within the rear-flank downdrafts of nontornadic and tornadic supercells. *Mon. Wea. Rev.*, **130**, 1692–1721, https://doi.org/10.1175/1520-0493(2002)130<1692:DSTOWT>2.0.CO;2.

——, ——, and ——, 2003: Tornadogenesis resulting from the transport of circulation by a downdraft: idealized numerical simulations. *J. Atmos. Sci.*, **60**, 795–823, https://doi.org/10.1175/1520-0469(2003)060<0795:TRFTTO>2.0.CO;2.

——, Y. Richardson, E. Rasmussen, J. Straka, R. Davies-Jones, and R. J. Trapp, 2008: Vortex lines within low-level mesocyclones obtained from pseudo-dual-Doppler radar observations. *Mon. Wea. Rev.*, **136**, 3513–3535, https://doi.org/10.1175/2008MWR2315.1.

Marquis, J., Y. Richardson, J. Wurman, and P. Markowski, 2008: Single- and dual-Doppler analysis of a tornadic vortex and surrounding storm-scale flow in the Crowell, Texas, supercell of 30 April 2000. *Mon. Wea. Rev.*, **136**, 5017–5043, https://doi.org/10.1175/2008MWR2442.1.

——, ——, P. Markowski, D. Dowell, and J. Wurman, 2012: Tornado maintenance investigated with high-resolution dual-Doppler and EnKF analysis. *Mon. Wea. Rev.*, **140**, 3–27, https://doi.org/10.1175/MWR-D-11-00025.1.

Rasmussen, E. N., J. M. Straka, R. Davies-Jones, C. A. Doswell III, F. H. Carr, M. D. Eilts, and D. R. MacGorman, 1994: Verification of the Origins of Rotation in Tornadoes Experiment: VORTEX. *Bull. Amer. Meteor. Soc.*, **75**, 995–1006, https://doi.org/10.1175/1520-0477(1994)075<0995:VOTOOR>2.0.CO;2.

Rotunno, R., and J. Klemp, 1985: On the rotation and propagation of simulated supercell thunderstorms. *J. Atmos. Sci.*, **42**, 271–292, https://doi.org/10.1175/1520-0469(1985)042<0271:OTRAPO>2.0.CO;2.

——, J. B. Klemp, and M. L. Weisman, 1988: A theory for strong, long-lived squall lines. *J. Atmos. Sci.*, **45**, 463–485, https://doi.org/10.1175/1520-0469(1988)045<0463:ATFSLL>2.0.CO;2.

Schroeder, J. L., and C. C. Weiss, 2008: Integrating research and education through measurement and analysis. *Bull. Amer. Meteor. Soc.*, **89**, 793–798, https://doi.org/10.1175/2008BAMS2287.1.

——, W. S. Burgett, K. B. Haynie, I. Sonmez, G. D. Skwira, A. L. Doggett, and J. W. Lipe, 2005: The West Texas Mesonet: A technical overview. *J. Atmos. Oceanic Technol.*, **22**, 211–222, https://doi.org/10.1175/JTECH-1690.1.

Simpson, J. E., 1969: A comparison between laboratory and atmospheric density currents. *Quart. J. Roy. Meteor. Soc.*, **95**, 758–765, https://doi.org/10.1002/qj.49709540609.

——, and R. E. Britter, 1980: A laboratory model of an atmospheric mesofront. *Quart. J. Roy. Meteor. Soc.*, **106**, 485–500, https://doi.org/10.1002/qj.49710644907.

Skinner, P. S., C. C. Weiss, M. M. French, H. B. Bluestein, P. M. Markowski, and Y. P. Richardson, 2014: VORTEX2 observations of a low-level mesocyclone with multiple internal rear-flank downdraft momentum surges in the 18 May 2010 Dumas, Texas, supercell. *Mon. Wea. Rev.*, **142**, 2935–2960, https://doi.org/10.1175/MWR-D-13-00240.1.

——, ——, L. J. Wicker, C. K. Potvin, and D.C. Dowell, 2015: Forcing mechanisms for an internal rear-flank downdraft momentum surge in the 18 May 2010 Dumas, Texas, supercell. *Mon. Wea. Rev.*, **143**, 4305–4330, https://doi.org/10.1175/MWR-D-15-0164.1.

Weiss, C. C., and J. L. Schroeder, 2008: StickNet: A new portable rapidly-deployable surface observation system. *24th Conf. on IIPS*, New Orleans, LA, Amer. Meteor. Soc., 4A.1, https://ams.confex.com/ams/88Annual/techprogram/paper_134047.htm.

——, D. C. Dowell, J. L. Schroeder, P. S. Skinner, A. E. Reinhart, P. M. Markowski, and Y. P. Richardson, 2015: A comparison of near-surface buoyancy and baroclinity across three VORTEX2 supercell intercepts. *Mon. Wea. Rev.*, **143**, 2736–2753, https://doi.org/10.1175/MWR-D-14-00307.1.

Xu, Q., 1992: Density currents in shear flows—A two-fluid model. *J. Atmos. Sci.*, **49**, 511–524, https://doi.org/10.1175/1520-0469(1992)049<0511:DCISFA>2.0.CO;2.

——, M. Xue, and K. K. Droegemeier, 1996: Numerical simulations of density currents in sheared environments within a vertically confined channel. *J. Atmos. Sci.*, **53**, 770–786, https://doi.org/10.1175/1520-0469(1996)053<0770:NSODCI>2.0.CO;2.

Xue, M., Q. Xu, and K. K. Droegemeier, 1997: A theoretical and numerical study of density currents in nonconstant shear flows. *J. Atmos. Sci.*, **54**, 1998–2019, https://doi.org/10.1175/1520-0469(1997)054<1998:ATANSO>2.0.CO;2.